## PAPER

# Modulating the d-band center of boron doped single-atom sites to boost the oxygen reduction reaction†

He Sun,‡[a] Mengfan Wang, [iD] ‡[b] Xinchuan Du,‡[a] Yu Jiao,[c] Sisi Liu, [iD] [b] Tao Qian, [iD] [b] Yichao Yan,[a] Chen Liu,[d] Min Liao,*[d] Qinghua Zhang,[e] Linxing Meng,[b] Lin Gu,[e] Jie Xiong [iD] *[a] and Chenglin Yan [iD] *[b]

The development of oxygen reduction reaction (ORR) catalysts with low overpotential is highly desirable but proves to be challenging. One promising way to improve the catalytic activity is to modulate the electronic structure of the catalyst; however, its impact on the intermediate adsorption kinetics remains poorly understood. Herein, a boron dopant was firstly reported to modulate the d-band center of a single-atom catalyst, enabling favorable adsorption kinetics and thus improved ORR performance. The optimized catalyst outperforms pure Fe–N–C and commercial Pt/C in a 0.1 M KOH medium, showing a half-wave potential of 0.933 V *versus* the reversible hydrogen electrode (*vs.* RHE) and ranking at the top of non-precious metal catalysts. First-principles calculations indicate the increased valence electrons and decreased magnetic moment of single-atom sites after B-doping. The modulated d-band center provides the system with favorable adsorption energy of oxygen and a much lower overpotential, thus greatly boosting the ORR performance.

## Introduction

The electrochemical oxygen reduction reaction (ORR) plays a key role in the development of next generation power supply systems including fuel cells[1] and metal–air batteries.[2] Platinum metal group-based materials are generally efficient catalysts for the ORR.[3] However, their scarcity and high cost hinder the commercialization of technologies involving the ORR. Hence, intensive efforts have been devoted to the search for low-cost and high-performance catalysts.[4–6] Iron-based materials represent a promising alternative, particularly given the fact that iron

and nitrogen co-doped carbon materials (Fe–N–C)[7–10] have exhibited comparable performance to the state-of-the-art Pt/C catalysts. However, there is still a need for better understanding the modulation of the electronic structure of high kinetic activity in Fe–N–C catalysts for further reducing the overpotential.

The high overpotential during the ORR can be linked to the difficulty in adsorbing oxygen molecules or due to the fact that the reaction intermediates are strongly bonded at the reversible potential.[11,12] For the Fe–N–C system, the adsorption behavior of iron as a generally recognized active site is not intrinsic, which can be regulated by changes in the bond length of Fe–N–C, the oxidation states of iron, and the chemical properties of the nearest heterogeneous doped atoms.[13,14] In particular, the adsorption energies of reaction intermediates would weaken monotonically with increasing number of valence electrons and decreasing oxidation state of the active sites.[15,16] Given the fact that the local average of the d-band electron energies of the transition metal suffices to describe the electronic effect,[17] a general correlation between adsorption energy and the shifting of the d-band center ($E_d$) can be obtained.[18] In this case, the intrinsic activity interacting with intermediates of the active site, namely the transition metal center, can be further improved by modulating the d-band electronic structure.[19,20] Doping heteroatoms is generally applied to realize electron modulation.[21] Among various dopants, B holds great potential to redistribute the inhomogeneous spin and charge densities induced by the coordination of metal and nitrogen atoms,[22]

[a]*State Key Laboratory of Electronic Thin Films and Integrated Devices, University of Electronic Science and Technology of China, Chengdu 610054, P. R. China. E-mail: jiexiong@uestc.edu.cn*

[b]*College of Energy, Key Laboratory of Advanced Carbon Materials and Wearable Energy Technologies of Jiangsu Province, Key Lab of Advanced Optical Manufacturing Technologies of Jiangsu Province, Key Lab of Modern Optical Technologies of Education Ministry of China, Soochow University, Suzhou 215006, P. R. China. E-mail: c.yan@suda.edu.cn*

[c]*School of Applied and Chemical Engineering, Xichang College, Xichang 615053, P. R. China*

[d]*Hunan Provincial Key Laboratory of Thin Film Materials and Devices, School of Materials Science and Engineering, Xiangtan University, Xiangtan 411105, P. R. China. E-mail: mliao@xtu.edu.cn*

[e]*Beijing National Laboratory for Condensed Matter Physics, Institute of Physics, Chinese Academy of Science, Beijing 100190, P. R. China*

† Electronic supplementary information (ESI) available. See DOI: 10.1039/c9ta06949f

‡ These authors contributed equally.

making the metal center more favorable for oxygen adsorption and thus resulting in enhanced ORR activity.

Herein, a boron dopant was introduced into the single-atom Fe–N–C system, aiming to modulate the Fe d-band center for favorable adsorption kinetics and therefore boost the ORR process. The optimized catalyst outperforms pure Fe–N–C and commercial Pt/C in a 0.1 M KOH medium, showing a half-wave potential of 0.933 V *versus* the reversible hydrogen electrode (*vs.* RHE) and ranking at the top of non-precious metal catalysts. The contribution of the favorable adsorption kinetics as a result of B doping to such extremely outstanding activity is verified by cyanide treatment, in which the B-doped Fe–N–C system is the worst affected after the coordination between iron and cyanide ions. First-principles calculations suggest increased valence electrons and decreased magnetic moment of Fe sites after B-doping. An appropriate adsorption energy of oxygen and a much lower overpotential can be obtained by the Fe d-band center modulation, thus providing the system with such superior ORR performance.

## Results

### Synthesis and characterization of the Fe$_{SA}$/B,N-CNT catalyst

The synthetic strategy of the proof-of-concept single-atom dispersed iron supported on boron and nitrogen-doped carbon nanotubes (Fe$_{SA}$/B,N-CNT) is shown in Fig. S1 (ESI†). The typical scanning electron microscopy (SEM, Fig. S2, ESI†) and transmission electron microscopy (TEM, Fig. 1a) images clearly illustrate the nanotube morphology without Fe aggregation. For comparison, the particulate phase of iron supported on nitrogen-doped carbon nanotubes (Fe$_{NP}$/N-CNT, Fig. S3, ESI†) and single-atom dispersed iron supported on nitrogen-doped carbon nanotubes (Fe$_{SA}$/N-CNT, Fig. S4, ESI†) were also prepared. The X-ray diffraction (XRD) pattern shows no sharp peaks corresponding to metallic Fe or other Fe species for Fe$_{SA}$/B,N-CNT and only two broad peaks assignable to graphitic carbon are observed (Fig. S5, ESI†), which is in consistent with

the $I_D/I_G$ value in Raman spectra (Fig. S6, ESI†).[23] Considering the exact Fe content of 0.46 wt% in Fe$_{SA}$/B,N-CNT as measured by inductively coupled plasma optical emission spectrometry (ICP-OES), which is investigated with the content of overall elements in Table S1,† aberration-corrected high-angle annular dark-field scanning transmission electron microscopy (AC HAADF-STEM) was thus utilized to elucidate the existing form of Fe at the atomic level. Fig. 1b exhibits evenly scattered isolated bright dots, indicating that the isolated single Fe atoms are well dispersed on the B,N-CNT support. The representative mapping images further demonstrate the uniform distribution of Fe, N, and B on the entire architecture (Fig. 1c).

The coordination environment and chemical state of the singly dispersed Fe can be confirmed by X-ray absorption fine structure (XAFS) analysis, including X-ray absorption near-edge structure (XANES) and extended X-ray absorption fine structure (EXAFS). Fig. 1d shows the Fe K-edge XANES spectra of Fe$_{SA}$/N-CNT and Fe$_{SA}$/B,N-CNT and their near-edge absorption energy are located between those of Fe$_2$O$_3$ and Fe Foil, indicating that the single Fe atoms in Fe$_{SA}$/B,N-CNT are much more positively charged than B-doped catalysts.[24] The Fourier transform (FT) $k^3$-weighted EXAFS curve of different samples are shown in Fig. 1e. Fe$_{SA}$/B,N-CNT only exhibits one obvious peak at about 1.52 Å assignable to the Fe–N scattering path, while no distinct Fe–Fe peak (2.2 Å) and Fe–B peak[25] (2.4 Å) are detected, unambiguously confirming the atomic dispersion of Fe stabilized by N atoms throughout the whole structure.[26] X-ray photoelectron spectroscopy (XPS) measurements were carried out to obtain the elemental information of C, N, and B (Fig. S7–S9, ESI†). The N 1s spectrum can be deconvoluted into four bands at 398.1, 398.9, 400.4, and 403.6 eV, corresponding to the pyridinic N, pyrrolic N, graphitic N, and N-oxide bonding structures, respectively,[27] in which pyridinic N and pyrrolic N serve as anchors for Fe atoms (Fig. S10, ESI†). The B 1s peak can be fitted with three different moieties, namely B–C, B–N, and B–O,[28] in which B–N bonding located at ~191.2 eV is the dominant one, indicating that B and N tend to exist as pairs (Fig. 1f). Moreover, Fe$_{SA}$/B,N-CNT possesses a highly open surface area and low volumetric density for exposure of active sites, making it an ideal catalyst for ORR applications (Fig. S11 and S12, ESI†).
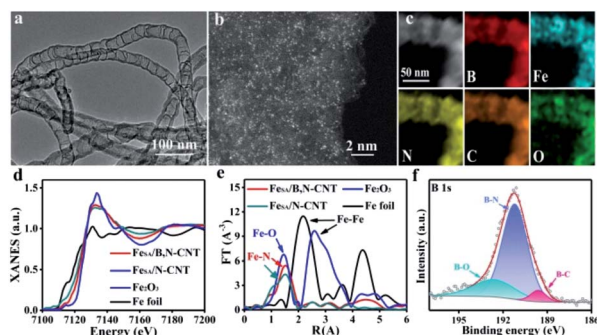
### Catalytic oxygen reduction activity and stability

The catalytic activity of Fe$_{SA}$/B,N-CNT was first evaluated by cyclic voltammetry (CV) measurements in N$_2$- and O$_2$-saturated 0.1 M KOH (Fig. S13, ESI†). In contrast to the N$_2$-saturated case, all samples display well-defined reduction peaks in the O$_2$-saturated solution. The strongest cathodic current as well as the most positive ORR peak potential are achieved by Fe$_{SA}$/B,N-CNT. The results indicate that Fe$_{SA}$/B,N-CNT possesses the best ORR activity, which is further verified by the linear sweep voltammetry (LSV) curves recorded on a rotating disk electrode (RDE) (Fig. S14, ESI†). In Fig. 2a, Fe$_{SA}$/B,N-CNT exhibits an unprecedented ORR activity, with the most positive half-wave potential ($E_{1/2}$) of 0.933 V *vs.* RHE, which is 60 mV more positive than that of commercial Pt/C ($E_{1/2} = 0.873$ V *vs.* RHE) and notably is the highest value among the reported values for non-precious metal
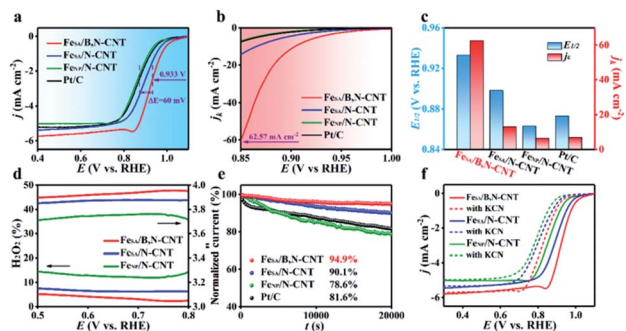


Fig. 1 Characterization of the Fe$_{SA}$/B,N-CNT catalyst. (a) TEM image of Fe$_{SA}$/B,N-CNT. Scale bar, 100 nm. (b) AC HAADF-STEM image of Fe$_{SA}$/B,N-CNT. Scale bar, 2 nm. (c) HAADF-STEM and corresponding elemental mapping images of Fe$_{SA}$/B,N-CNT. Scale bar, 50 nm. (d) XANES spectra and (e) Fourier transform EXAFS spectra at the Fe K-edge of Fe$_{SA}$/N-CNT, Fe$_{SA}$/B,N-CNT, Fe$_2$O$_3$, and Fe foil. (f) High-resolution XPS spectra of B 1s of Fe$_{SA}$/B,N-CNT.

This journal is © The Royal Society of Chemistry 2019

*J. Mater. Chem. A*, 2019, **7**, 20952–20957 | **20953**

**Fig. 2** Electrocatalytic performance of the $Fe_{SA}/B,N\text{-}CNT$ catalysts. (a) ORR polarization curves and (b) kinetic current density of different samples in $O_2$-saturated 0.1 M KOH. (c) Comparison of $E_{1/2}$ and $j_k$ at 0.85 V vs. RHE for different catalysts. (d) $H_2O_2$ yield and electron transfer number plots from 0.5 to 0.8 V vs. RHE. (e) Chronoamperometric curves of different samples in $O_2$-saturated 0.1 M KOH. (f) Effects of $CN^-$ ions (10 mM) on the ORR activities of different catalysts in 0.1 M KOH.

catalysts (Table S2, ESI†). The exact kinetic parameters including kinetic current density ($j_k$) and electron transfer number ($n$) were analyzed on the basis of Koutecky–Levich equations. $Fe_{SA}/B,N\text{-}CNT$ shows a highest $j_k$ of 62.57 mA cm$^{-2}$ at 0.85 V vs. RHE (Fig. 2b), about 9 times that of commercial Pt/C (6.98 mA cm$^{-2}$) in 0.1 M KOH (Fig. 2c). Rotating ring disk electrode (RRDE) tests were then conducted to study the hydrogen peroxide yields and electron transfer mechanism. Fig. 2d reveals that the peroxide yield of $Fe_{SA}/B,N\text{-}CNT$ determined from the ring current remains below 5.2% and the average $n$ equals 3.95 over the potential range of 0.50–0.80 V vs. RHE, suggesting a four-electron pathway in alkaline medium and apparently superior ORR kinetics. The methanol tolerance was confirmed by instantaneously adding 3 M methanol into $O_2$-saturated 0.1 M KOH during chronoamperometric measurements. The commercial Pt/C system exhibits a sharp current decrease in the $i$–$t$ curve due to the oxidation of methanol. As for $Fe_{SA}/B,N\text{-}CNT$, almost no oscillation is observed, demonstrating its excellent tolerance to methanol crossover (Fig. S15, ESI†). In addition, the $Fe_{SA}/B,N\text{-}CNT$ catalyst shows a much better durability than commercial Pt/C and other counterparts in the alkaline medium during long-term operation, with only 5.1% activity attenuation after 20 000 s of operation (Fig. 2e and S16, ESI†). A careful examination of the HAADF-STEM image, XRD, Raman and elemental mapping images confirms the excellent structural stability of $Fe_{SA}/B,N\text{-}CNT$, in which the atomically dispersed Fe atoms remain unchanged and Fe, N, and B are still uniformly distributed on the support (Fig. S17, S18, and S19, ESI†).

## Discussion

To gain mechanistic insights into the outstanding electrocatalytic activity of $Fe_{SA}/B,N\text{-}CNT$ for the ORR, the Tafel plots from the corresponding LSV curves in Fig. 2a are used to analyze the catalytic kinetics (Fig. S20, ESI†). $Fe_{SA}/B,N\text{-}CNT$ exhibits a Tafel slope of 61.9 mV dec$^{-1}$, which is lower than that of

commercial Pt/C and other counterparts, thus indicating its superior kinetics toward the ORR. Besides, such a value suggests that the transfer of the first electron on $Fe_{SA}/B,N\text{-}CNT$ is the rate-determining step in the catalytic process under Temkin conditions for the adsorption of intermediates.[29] The favorable kinetics of $Fe_{SA}/B,N\text{-}CNT$ for the ORR can be further confirmed by the electrochemical impedance spectroscopy (EIS) and electrochemical surface area (ECSA) results. Fig. S21 (ESI†) shows the Nyquist plots of the EIS spectra and it can be seen that $Fe_{SA}/B,N\text{-}CNT$ exhibits the smallest semicircle diameter in the high frequency region and the largest slope of the straight line in the low frequency region, indicating its lowest charge transfer resistance and ion diffusion resistance.[30] The ECSA can be estimated from the double layer capacitance ($C_{dl}$). $Fe_{SA}/B,N\text{-}CNT$ presents a larger $C_{dl}$ of 13.06 mF cm$^{-2}$ than $Fe_{SA}/N\text{-}CNT$ or $Fe_{NP}/N\text{-}CNT$, implying its much faster electron and mass transport kinetics (Fig. S22, ESI†).

The superior performance of $Fe_{SA}/B,N\text{-}CNT$ should be cooperatively governed by the number of active sites and the intrinsic activity of each site. To clarify the contribution of these two factors, poisoning experiments of cyanide ions ($CN^-$) on the ORR performance were conducted since $CN^-$ is well known to forcefully coordinate with iron and thus poison the iron-containing catalytic sites[31] (Fig. 2f). As expected, upon adding 10 mM KCN to 0.1 M KOH, the half-wave potentials of $Fe_{NP}/N\text{-}CNT$ and $Fe_{SA}/N\text{-}CNT$ negatively shifted by 75 mV and 85 mV, respectively, corresponding to the fact that $Fe_{SA}/N\text{-}CNT$ obviously exposes more metal-centered active sites than $Fe_{NP}/N\text{-}CNT$. As for $Fe_{SA}/B,N\text{-}CNT$, the activity shows a more serious decrease of 95 mV in the half-wave potential, clearly indicating that the intrinsic activity of Fe–N–B is more favorable for the ORR than that of pure Fe–N.

The critical role played by B dopants is then investigated by density functional theory (DFT) calculations. We first compare the formation energies ($E_f$) of various possible structures by using the (6, 6) CNT model (Fig. S23, ESI†) for gaining insight into the stability of different B-doped $Fe_{SA}/N\text{-}CNT$ structures. Among them, the smallest $E_f$ ($E_f = -4.06$ eV) is obtained by the two opposite B atoms in different hexatomic rings ($B_2$-opp-hex), which means that the favorite reaction is the formation of $Fe_{SA}/B,N\text{-}CNT$. Subsequently, the charge density difference, projected density of states (PDOS) and Mulliken population analysis are used to capture the essential electronic structure of B-doped systems.[32,33] The d-band center of the catalysts can be determined to be $-3.90$ eV for $Fe_{SA}/N\text{-}CNT$, $-2.91$ eV for $Fe_{SA}/B_1,N\text{-}CNT$, and $-2.58$ eV for $Fe_{SA}/B_2,N\text{-}CNT$. Clearly, boron doping in $Fe_{SA}/N\text{-}CNT$ would efficiently increase the d-band center of the catalyst. The more the boron dopants, the lower the d-band center is. Combined with the free energy data, it can be concluded that the decreased d-band center of the catalyst greatly contributes to the decreased adsorption energy of $O_2$, and thus the reaction barrier (Fig. S24, ESI†). For the pristine $Fe_{SA}/N\text{-}CNT$ model, its charge density displays enhanced orbital hybridization between Fe and N compared with the π-electron conjugated system, forming a coordination bond in the $FeN_4$ moiety (Fig. 3a). The occurrence of significant charge redistribution induced by B doping is indicated in the isosurface plots
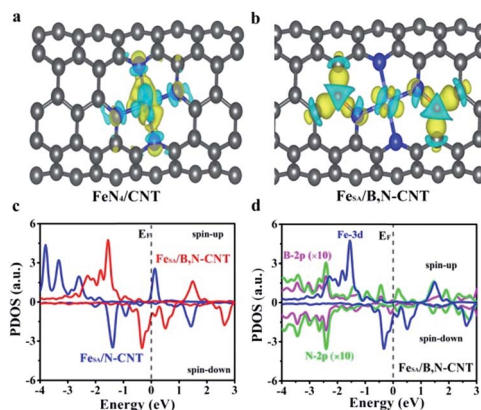
**20954** | *J. Mater. Chem. A*, 2019, **7**, 20952–20957

This journal is © The Royal Society of Chemistry 2019

**Fig. 3** DFT calculations of the modified d-band center of the B-doped FeN$_4$ models. The isosurfaces (0.01 e Å$^{-3}$) of charge density variation in (a) FeN$_4$/CNT and (b) Fe$_{SA}$/B,N-CNT. Light blue area represents charge density decrease ($\Delta\rho < 0$) and yellow area denotes charge density increase ($\Delta\rho > 0$). Purple, blue, pink, and grey represent Fe, N, B, and C atoms, respectively. (c) The PDOS for the 3d orbitals of the active Fe atoms in Fe$_{SA}$/N-CNT and Fe$_{SA}$/B,N-CNT. (d) The PDOS for the Fe-3d, N-2p and B-2p orbitals in Fe$_{SA}$/B,N-CNT.



**Fig. 4** Free energy diagram. (a) Front (up) and top (down) views of the optimized geometries of ORR intermediates in the Fe$_{SA}$/B,N-CNT system: OO*, HOO*, O* and HO*. Purple, blue, pink, grey, red, and white spheres represent Fe, N, B, C, O, and H, respectively. (b) The free-energy landscape for Fe$_{NP}$/N-CNT, Fe$_{SA}$/N-CNT, and Fe$_{SA}$/B,N-CNT during the ORR under alkaline conditions at $U = 0$ V. (c) The correlation of the ORR overpotentials with the O$_2$ adsorption energies for Fe$_{NP}$C/CNT, Fe$_{SA}$/N-CNT, and Fe$_{SA}$/B,N-CNT.

of charge density variation, with a smaller amount of electron cloud shift away from N to B (Fig. 3b and S25, ESI†), leading to a modulated d-band center of Fe. Specifically, as shown in Fig. 3c and d, all models show metallic features with the PDOS crossing over the Fermi level. For the un-doped system (Fe$_{SA}$/N-CNT), the Fe-3d orbitals occupy the low-lying states, in the energy range from −3.95 to −0.78 eV, due to the strong hybridization of the bonded N atoms. With B doping (Fe$_{SA}$/B,N-CNT), the interaction between Fe-3d and N-2p states away from the Fermi level is gradually diminished and the down-spin resonance is obviously enhanced and shifts towards higher energy.

The Gibbs free energy of each ORR step (Fig. 4a) was then calculated and several key results can be seen from these calculations (Fig. 4b). While the O$_2$ adsorption on Fe$_{NP}$/N-CNT (Fig. S26, ESI†) is hindered by a thermodynamic energy barrier of 0.3 eV at $U = 0$ V, the same process on Fe$_{NP}$/N-CNT, Fe$_{SA}$/N-CNT, and Fe$_{SA}$/B,N-CNT goes downhill, corroborating that all electron transfer steps are exothermic in the ORR (Table S3, ESI†). For Fe$_{SA}$/N-CNT, the most sluggish reaction step is the hydrogenation of adsorbed O$_2$, which is the rate-limiting step for the ORR. For Fe$_{SA}$/B,N-CNT, the fourth electron transfer reaction is the rate-limiting step and apparently, Fe$_{SA}$/B,N-CNT displays better catalytic performance than Fe$_{SA}$/N-CNT for the ORR.[34,35] Based on the free energy and the equation of minimum thermodynamic overpotential,[36] the ORR overpotentials of different models are estimated and a rough volcano plot of the ORR overpotential against adsorption energy is presented in Fig. 4c. On the weaker $E_{ads}$ side, the lower adsorption energy usually leads to difficulty in adsorbing the oxygen so that the ORR is mainly limited by the first adsorption step (O$_2$ + * → OO*, * represents an adsorption site). On the stronger $E_{ads}$ side, the ORR is mainly determined by the OH* reduction step, which is suppressed by strong oxygen
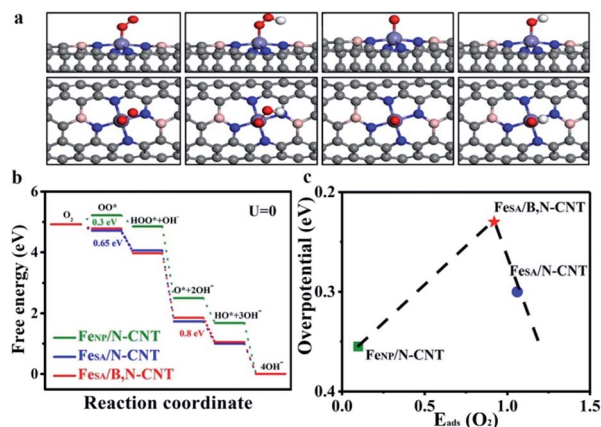
adsorption. As for Fe$_{SA}$/B,N-CNT, it displays a much lower overpotential (0.23 V) than other models and possesses an appropriate adsorption energy of oxygen ($E_{ads} = 0.92$ eV). The free energetics of the ORR obtained from the DFT calculations rationalize the experimental measurements and we can conclude that a favorable surface electronic environment can be produced by the B-doped FeN$_4$ system to boost the ORR performance.

Considering the desirable OER performance (Fig. S27, ESI†), Fe$_{SA}$/B,N-CNT was used as an air catalyst for a rechargeable Zn–air battery. As shown in Fig. 5a, the Fe$_{SA}$/B,N-CNT-based battery
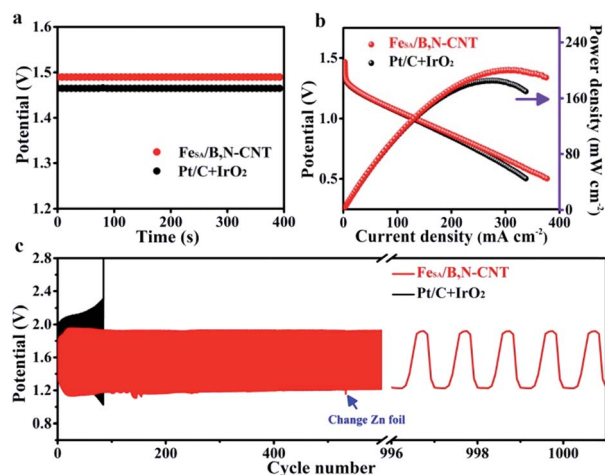


**Fig. 5** (a) Open-circuit plots of zinc–air batteries with Fe$_{SA}$/B,N-CNT and Pt/C + IrO$_2$ as cathodes in aqueous solution. (b) Discharge polarization curves and the corresponding power density plots. (c) Galvanostatic cycling profiles of zinc–air batteries with Fe$_{SA}$/B,N-CNT and Pt/C + IrO$_2$ at a current density of 5 mA cm$^{-2}$.

This journal is © The Royal Society of Chemistry 2019

J. Mater. Chem. A, 2019, **7**, 20952–20957 | **20955**

delivers an open-circuit voltage of 1.49 V. Fig. 5b shows a maximum power density of 200 mW cm$^{-2}$ of Fe$_{SA}$/B,N-CNT, outperforming the noble-metal couterpart. After 1000 cycles (10 minutes per cycle) at a current density of 5 mA cm$^{-2}$, the rechargeable Zn–air battery exhibits stable charge/discharge plateaus of 1.92 and 1.22 V, respectively.

## Conclusions

In summary, d-band center modulation induced by boron doping has been experimentally and theoretically demonstrated to enable favorable oxygen adsorption kinetics for Fe–N active sites and thus boost the ORR process. The proof-of-concept Fe$_{SA}$/B,N-CNT exhibits a superior ORR activity with a half-wave potential of 0.933 V *vs.* RHE and a $j_k$ of 62.57 mA cm$^{-2}$ at 0.85 V *vs.* RHE in 0.1 M KOH, outperforming not only commercial Pt/C but also all non-precious metal electrocatalysts reported to date. Evidenced by the Tafel slope of the catalyst as well as the EIS and ECSA results, the ORR kinetics are favorable. Cyanide treatment measurements verify the advantages of the maximum atom efficiency of the single-atom catalyst and the enhanced intrinsic activity induced by B doping as suggested by the increasing activity deterioration degree from Fe$_{SA}$/B,N-CNT to Fe$_{SA}$/N-CNT to Fe$_{NP}$/N-CNT. DFT calculations confirm that the relatively low electronegativity of B can transfer electrons from N to B, increasing the valence electrons and decreasing the magnetic moment of Fe, which could greatly enhance the oxygen adsorption and contribute to the whole oxygen reduction process. As a result, the rate-limiting step of the optimized configuration is positively shifted to the fourth electron transfer reaction. Such appropriate adsorption energy of oxygen and much lower overpotential agree well with the experimental results, highlighting the contribution of d-band center modulation in producing favorable oxygen adsorption kinetics and thereby boosting the ORR performance.

## Author contributions

H. S., M. W., and X. D. contributed equally to this work. H. S. and M. W. conceived the idea. H. S. and X. D. carried out the sample synthesis, characterization, performance measurement and manuscript writing. S. L., Y. J., T. Q., and Y. Y. helped with discussion. Q. Z., and L. G. helped with the AC HAADF-STEM measurement. L. M. helped with the XAFS measurements and discussion. C. L. and M. L. edited the manuscript and J. X. and C. Y. revised the manuscript.

## Conflicts of interest

There are no conflicts to declare.

## Acknowledgements

## Notes and references

1 M. K. Debe, *Nature*, 2012, **486**, 43–51.
2 Z. Peng, S. A. Freunberger, Y. Chen and P. G. Bruce, *Science*, 2012, **337**, 563–566.
3 V. R. Stamenkovic, F. Ben, M. Bongjin Simon, W. Guofeng, P. N. Ross, C. A. Lucas and N. M. Marković, *Science*, 2007, **315**, 493–497.
4 Y. R. Liang, C. Z. Zhao, H. Yuan, Y. Chen, W. C. Zhang, J. Q. Huang, D. S. Yu, Y. L. Liu, M. M. Titirici, Y. L. Chueh, H. J. Yu and Q. Zhang, *InfoMat*, 2019, **1**, 6–32.
5 Y. R. Li, Q. H. Xiong, Y. C. Liu, J. H. Hao, R. Morandotti and C. Diederichs, *InfoMat*, 2019, **1**, 4–5.
6 S. Liu, M. Wang, X. Sun, N. Xu, J. Liu, Y. Wang, T. Qian and C. Yan, *Adv. Mater.*, 2018, **30**, 1704898.
7 M. Wang, S. Liu, N. Xu, T. Qian and C. Yan, *Adv. Sustainable Syst.*, 2017, **1**, 1700085.
8 M. Wang, W. Wang, T. Qian, S. Liu, Y. Li, Z. Hou, J. B. Goodenough, P. M. Ajayan and C. Yan, *Adv. Mater.*, 2019, **31**, 1803339.
9 S. Liu, M. Wang, T. Qian, J. Liu and C. Yan, *ACS Appl. Mater. Interfaces*, 2019, **11**, 20056–20063.
10 Z. Miao, X. Wang, M.-C. Tsai, Q. Jin, J. Liang, F. Ma, T. Wang, S. Zheng, B.-J. Hwang, Y. Huang, S. Guo and Q. Li, *Adv. Energy Mater.*, 2018, **8**, 1801226.
11 J. H. Zagal and M. T. Koper, *Angew. Chem., Int. Ed.*, 2016, **55**, 14510–14521.
12 J. K. Nørskov, J. Rossmeisl, A. Logadottir, L. Lindqvist, J. R. Kitchin, T. Bligaard and H. J. K. Jonsson, *J. Phys. Chem. B*, 2004, **108**, 17886–17892.
13 C. V. Federico, M. José Ignacio and R. Jan, *Phys. Chem. Chem. Phys.*, 2011, **13**, 15639–15643.
14 M. Wang, S. Liu, T. Qian, J. Liu, J. Zhou, H. Ji, J. Xiong, J. Zhong and C. Yan, *Nat. Commun.*, 2019, **10**, 341.
15 F. Calle-Vallejo, N. G. Inoglu, H. Y. Su, J. I. Martínez and J. Rossmeisl, *Chem. Sci.*, 2013, **4**, 1245–1249.
16 Y. Zhou, F. Che, L. Min, C. Zou, Z. Liang, P. D. Luna, H. Yuan, J. Li, Z. Wang and H. Xie, *Nat. Chem.*, 2018, **10**, 974–980.
17 B. Hammer and J. K. Nørskov, *Adv. Catal.*, 2000, **31**, 71–129.
18 M. Mavrikakis, B. Hammer and J. K. Nørskov, *Phys. Rev. Lett.*, 1998, **81**, 2819–2822.
19 Y. Han, Y. Wang, R. Xu, W. Chen and Y. Li, *Energy Environ. Sci.*, 2018, **11**, 2348–2352.
20 I. E. L. Stephens, A. S. Bondarenko, U. Gronbjerg, J. Rossmeisl and I. Chorkendorff, *Energy Environ. Sci.*, 2012, **5**, 6744–6762.
21 Q. Li, W. Chen, H. Xiao, Y. Gong, Z. Li, L. Zheng, X. Zheng, W. Yan, W. C. Cheong and R. Shen, *Adv. Mater.*, 2018, **30**, 1800588.
22 K. Yuan, S. Sfaelou, M. Qiu, D. Lützenkirchen-Hecht, X. Zhuang, Y. Chen, C. Yuan, X. Feng and U. Scherf, *ACS Energy Lett.*, 2017, **3**, 252–260.
23 Y. Chen, S. Ji, Y. Wang, J. Dong, W. Chen, Z. Li, R. Shen, L. Zheng, Z. Zhuang, D. Wang and Y. Li, *Angew. Chem., Int. Ed.*, 2017, **129**, 6937–6941.

20956 | *J. Mater. Chem. A*, 2019, **7**, 20952–20957

This journal is © The Royal Society of Chemistry 2019

24  L. Yang, D. J. Cheng, H. X. Xu, X. F. Zeng, X. Wan, J. L. Shui, Z. H. Xiang and D. P. Cao, *Proc. Natl. Acad. Sci. U. S. A.*, 2018, **115**, 6626–6631.

25  S. Rades, A. Kornowski, H. Weller and B. Albert, *ChemPhysChem*, 2011, **12**, 1756–1760.

26  H. Fei, J. Dong, Y. Feng, C. S. Allen, C. Wan, B. Volosskiy, M. Li, Z. Zhao, Y. Wang and H. Sun, *Nat. Catal.*, 2018, **1**, 63–72.

27  L. Lai, J. R. Potts, D. Zhan, L. Wang, C. K. Poh, C. Tang, H. Gong, Z. Shen, J. Lin and R. S. Ruoff, *Energy Environ. Sci.*, 2012, **5**, 7936–7942.

28  J. Jin, F. Pan, L. Jiang, X. Fu, A. Liang, Z. Wei, J. Zhang and G. Sun, *ACS Nano*, 2014, **8**, 3313–3321.

29  B. Hu, Z. Wu, S. Chu, H. Zhu and S. Yu, *Energy Environ. Sci.*, 2018, **11**, 2208–2215.

30  Z. Li, M. Shao, Z. Lei, Q. Yang, Z. Cong, W. Min, D. G. Evans and D. Xue, *Nano Energy*, 2016, **25**, 100–109.

31  W. H. Niu, L. G. Li, X. J. Liu, N. Wang, J. Liu, W. J. Zhou, Z. H. Tang and S. W. Chen, *J. Am. Chem. Soc.*, 2015, **137**, 5555–5562.

32  R. S. Mulliken, *J. Chem. Phys.*, 1955, **23**, 1833–1840.

33  B. Hammer and J. K. Nørskov, *Surf. Sci.*, 1995, **343**, 211–220.

34  A. B. A. Anderson and R. A. S. Sidik, *J. Phys. Chem. B*, 2004, **108**, 5031–5035.

35  C. Y. Su, H. Cheng, W. Li, Z. Q. Liu and T. Y. Ma, *Adv. Energy Mater.*, 2017, **7**, 1602420.

36  M. T. M. Koper, *Chem. Sci.*, 2014, **44**, 2710–2723.